First Field Validation of a New VNIR–SWIR-Based Six-Band Multi-Camera System for UAVs over Winter Wheat

Alexander Jenal [1], Fabian Reddig [2], Andreas Bolten [2], Leon Vehlken [2], Hubert Hüging [3], Thuy Huu Nguyen [3], Jens Bongartz [1], Georg Bareth [2]

[1] Application Center for Machine Learning and Sensor Technologies, University of Applied Sciences Koblenz, Germany – (alexander.jenal, bongartz)@hs-koblenz.de
[2] Institute of Geography, GIS & Remote Sensing Group, University of Cologne, Germany – (andreas.bolten, fabian.reddig, lvehlke1, g.bareth)@uni-koeln.de
[3] Institute of Crop Science and Resource Conservation (INRES), University of Bonn, Germany – (h.hueging, tngu)@uni-bonn.de

Keywords: shortwave infrared, multispectral, empirical line calibration, calibration/validation, precision agriculture, crop monitoring.

Abstract

Shortwave infrared (SWIR) UAV imaging remains uncommon despite its sensitivity to canopy water and protein. We report, to our knowledge, the first field validation of a six-band, simultaneously exposed VNIR/SWIR multicamera for plot-scale winter wheat. The payload used narrow bandpass filters at 910, 980, 1100, 1200, 1510, and 1650 nm (FWHM 10–12 nm) and was flown at 30 m AGL, yielding 4 cm GSD. Radiometric calibration used in-flight empirical line calibration with an in-scene gray panel set, followed by independent validation on a material-distinct gray set. ASD spectroradiometer measurements were convolved with Gaussian proxy spectral response functions matched to the nominal filter passbands. Empirical line fits were near-perfect (R2 ≈ 1.000; RMSE = 0.003–0.009). Independent panel validation showed near-unity slopes for five bands from 980–1650 nm (R2 = 0.998–0.999; RMSE = 0.005–0.013). Across 36 canopy plot ROIs, camera-to-ASD agreement remained strong for five bands, with slopes of 0.943–1.079, R^2 = 0.58–0.85, and RMSE = 0.010–0.023. Two SWIR normalized ratio indices showed tight cross-sensor agreement: NRI[1100,1200] ($R^2 \approx 0.93$; RMSE ≈ 0.010) and NRI[1650,1510] ($R^2 \approx 0.90$; RMSE ≈ 0.017–0.018). Post-hoc filter transmittance measurements revealed secondary long-wavelength throughput in the 910 nm channel, causing compressed slopes and elevated error (MAPE ≈ 33%); this band was excluded from accuracy claims. Panel-anchored, bandpass-aware calibration enables quantitative UAV SWIR reflectance and robust SWIR indices for precision agriculture applications. The workflow also identifies hardware-specific failure modes, supporting reproducible validation and informed redesign of filter-reconfigurable SWIR payloads.

1. Introduction

Uncrewed aerial vehicles (UAVs) with multi- and hyperspectral sensors have transformed plot-scale phenotyping and precision agriculture by providing reflectance products and vegetation indices at centimeter-level resolution (Maes and Steppe, 2019; Hunt and Daughtry, 2018; Yang et al., 2017). Although visible-near-infrared (VNIR) systems dominate (Aasen et al., 2018), broad-band vegetation indices can saturate in dense canopies, limiting sensitivity to biomass and canopy traits when crops such as winter wheat require differentiated management decisions for water status and grain protein assessment. This saturation problem is well documented in high-density vegetation and has motivated narrow-band approaches that better preserve sensitivity under dense cover (Mutanga and Skidmore, 2004; Mutanga et al., 2023). Shortwave infrared (SWIR; conventionally 1000–2500 nm) and adjacent NIR-SWIR wavelengths contain water absorption features near 970, 1200, and 1450 nm and protein-sensitive bands at 1510 and 1650 nm. Water-band indices are especially attractive in this context because they can probe more deeply into thick canopies than chlorophyll-dominated VNIR indices, and near- and shortwave infrared combinations such as NDWI have shown reduced susceptibility to saturation at high LAI during vegetation water content upscaling (Sims and Gamon, 2003; Anderson et al., 2004).

We targeted six narrow bands between 910 and 1650 nm using an enhanced indium gallium arsenide (InGaAs) sensor array. Although the hardware is filter-reconfigurable across the detector's 400 to 1700 nm range, the validated configuration presented herein is concentrated in the NIR/SWIR domain, with compliant operational bands between 980 and 1650 nm.

InGaAs sensors are advantageous for vegetation monitoring, as these channels remain responsive at high leaf area indices (LAI) (Gao, 1996; Herrmann et al., 2010; Berger et al., 2020; Lee et al., 2024). However, UAV-based SWIR implementation remains rare because of the weight and cost constraints of InGaAs sensors. This agronomic relevance is reinforced by recent spaceborne crop-monitoring studies showing that PRISMA SWIR narrow bands and Sentinel-2 red-edge/NIR bands are among the top-performing spectral regions for field-level biomass and yield estimation across major crops, including wheat (Marshall et al., 2022). Realizing this potential at the UAV scale requires rigorous radiometric calibration and cross-sensor validation for scientific and operational use (Nansen et al., 2023; Lu et al., 2020). The empirical line calibration (ELC) with in-scene reflectance panels (Daniels et al., 2023) and spectral-response-function (SRF) harmonization for cross-sensor comparison represents best practice in quantitative UAV imaging (Chander et al., 2013; Cundill et al., 2015; Trishchenko et al., 2002; Thompson et al., 2018).

Building on UAV VNIR–SWIR advances (Honkavaara et al., 2016; Jenal et al., 2019), we present a six-camera VNIR–SWIR array exposing six bands simultaneously, validate it with an inflight ELC and independent panel set, and diagnose 910 nm out-of-band leakage. A key feature is its application-specific adaptability via interchangeable bandpass filters: wavelengths and passband widths can be reconfigured within the detector sensitivity range to target scenario-dependent features (e.g., water-sensitive bands, protein-related overtones, or task-specific atmospheric windows) without altering mechanical integration or photogrammetric workflow. This study contributes (i) a panel-anchored, SRF-aware calibration/validation protocol for plot-

This contribution has been peer-reviewed. The double-blind peer-review was conducted on the basis of the full paper.
https://doi.org/10.5194/isprs-annals-XI-1-2026-61-2026

scale UAV VNIR–SWIR imaging; (ii) quantitative evidence of near-unity camera-spectroradiometer agreement for five bands between 980 and 1650 nm; (iii) demonstration of two SWIR normalized ratio indices with high cross-sensor consistency (Koppe et al., 2010); and (iv) a transparent diagnosis and engineering remedy for a non-compliant 910 nm channel. This study aligns with priorities on UAV platforms, sensors, and calibration/validation and extends prior VNIR–SWIR UAV developments in agronomic contexts (Chakhvashvili et al., 2024; Oliveira et al., 2023). The validation is based on one winter wheat experimental site (Campus Klein-Altendorf, University of Bonn, Germany) and one campaign; thus, we quantify the performance under the tested conditions and discuss generalization and next-step multi-crop evaluation in the Discussion and Outlook.

2. Camera System, Study Area, and Data Workflow

Figure 1 shows the imaging payload, and Table 1 summarizes the filter configuration used in the field campaign, along with the shared camera specifications of the six-channel system. The payload is based on an earlier two-band SWIR camera system (Jenal et al., 2019) and extends it to a rigid six-camera (1.3 MP each) enhanced-InGaAs array with a detector sensitivity range of 400–1700 nm and interchangeable narrow bandpass filters (Jenal et al., 2024). For the present experiment, the deployed filters were centered at 910, 980, 1100, 1200, 1510, and 1650 nm, with nominal FWHM values of 10–12 nm. The modular design allows for application-specific reconfiguration of the wavelength position and bandwidth, whereas simultaneous exposure of all six channels minimizes inter-band temporal offsets caused by changing illumination, platform motion, or canopy movement during flight.

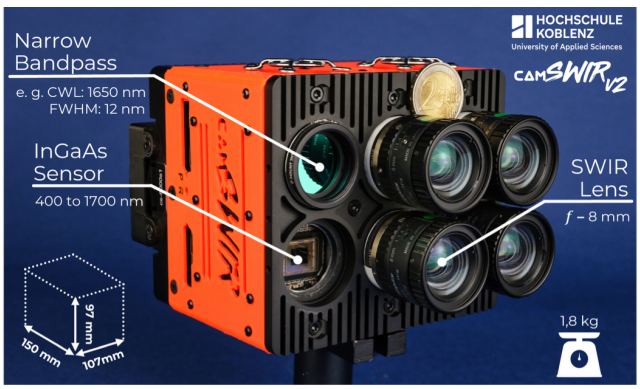

Figure 1. Front view of the six-band enhanced InGaAs VNIR–SWIR multispectral multicamera payload “camSWIRv2” used in the UAV campaign.

Field data were collected over a temperate winter wheat experiment at Campus Klein-Altendorf (University of Bonn, Germany) during the 2023/2024 growing season (Figure 2). The trial followed a split-plot design with five replicate blocks (rows), each subdivided into plots of six wheat cultivars under three nitrogen fertilizer levels (0, 120, and 240 kg N ha^{-1}), yielding 18 plots per row. Individual plots measured 7 × 1.5 m. The randomized layout and management of the experiment provided a realistic range of canopy conditions for testing radiometric transfer and cross-sensor consistency under agronomic field conditions.

For validation, 36 plots in rows 2 and 4 (Figure 2a) were selected for spectral sampling and camera–ASD comparison. Twelve ground control points (GCPs) were distributed across the field and surveyed with real-time kinematic Global Navigation Satellite System (RTK GNSS) measurements to support accurate georeferencing. Calibration-validation independence was ensured using two distinct in-scene reflectance target sets (Figure 2b). RAC-1 comprised five 1×1 m Lambertian panels spanning 5-95% reflectance for empirical line calibration (ELC). UzK-1 comprised six 0.8×0.8 m coated near-Lambertian aluminum panels used exclusively for independent validation. Because UzK-1 differed from RAC-1 in terms of material, coating, and size, this design provides a stricter transfer test than a holdout on the same target family and allows screening for material-specific bias in the radiometric transfer (Bruegge, 1993; Schunke et al., 2023).

Applied Filters		Image Sensor Characteristics	
CWL	**FWHM**	**Parameter**	**Value**
910 nm	10 nm	Sensor	InGaAs
980 nm	10 nm	Spectral Response	400 to 1700 nm
1100 nm	10 nm	Pixel Size	5×5 µm
1200 nm	10 nm	Resolution (H×V)	1296×1032
1510 nm	12 nm	Shutter	global
1650 nm	12 nm	Bit depth	12–bit

Table 1. Filter configuration and shared hardware specifications of the six-channel enhanced-InGaAs VNIR–SWIR multicamera used in this study. The left block lists the center wavelength (CWL) and full width at half maximum (FWHM) of the six narrow bandpass filters deployed during the winter wheat campaign. The right block lists image sensor characteristics common to all six simultaneously exposed channels, including detector type, spectral sensitivity, pixel pitch, image format, shutter mode, and radiometric resolution. The right-hand entries are system-wide properties and therefore apply equally to all six bands

During the UAV campaign, which was conducted near solar noon under clear-sky conditions, canopy and panel spectra were measured with an ASD FieldSpec 4 High-Res spectroradiometer (Malvern Panalytical Ltd., Malvern, Worcestershire, UK; spectral range 350–2500 nm, 1 nm sampling). The panels were measured in situ for quality assurance only; however, these in-field ASD panel readings were not used in the ELC fits or subsequent panel-based validation. Instead, both the ELC and validation referenced pre-characterized, laboratory-traceable panel reflectance factors obtained prior to the campaign. This decouples the radiance-to-reflectance transfer from the spectroradiometer later used for the camera–ASD cross-sensor comparison and avoids a closed-loop dependency, at the cost of a slightly more conservative error budget.

UAV image acquisition was performed with a custom octocopter at approximately 30 m above ground level, resulting in a ground sample distance of approximately 4 cm with an 8 mm prime lens. Each channel was processed independently in a structure-from-motion/photogrammetric workflow (Metashape Professional, version 2.1.2 build 18358; Agisoft LLC) to generate georeferenced per-band reflectance orthomosaics. The six derived mosaics are shown in Figure 3. They consistently preserve the split-plot pattern across bands and form the spatial basis for the ROI-based extraction of panel and canopy reflectance.

Because all six channels were recorded simultaneously rather than sequentially, the dataset was less sensitive to short-term changes in irradiance, wind-driven canopy motion, and platform attitude during acquisition. This is advantageous for narrowband multicamera validation because small acquisition-time offsets can propagate into band-to-band inconsistencies and ratio index noise (Aasen et al., 2018; Honkavaara et al., 2016).

This contribution has been peer-reviewed. The double-blind peer-review was conducted on the basis of the full paper.
https://doi.org/10.5194/isprs-annals-XI-1-2026-61-2026 | © Author(s) 2026. CC BY 4.0 License.

ASD reflectance factors were obtained using standard field spectroscopy, that is, by converting canopy and panel radiance spectra to reflectance with a calibrated white reference standard measured during the campaign to compensate for illumination changes. For the image-based analyses, mean DN/reflectance values were extracted from homogeneous regions of interest (ROIs) in the orthomosaics. Panel ROIs were placed centrally to exclude edges, shadowing, and border effects, whereas plot ROIs were placed within the canopy interior to avoid plot borders and mixed soil/background pixels. Identical ROI definitions were used across bands so that cross-band comparisons and index calculations were not confounded by differing sampling geometry or mixed pixels. The dashed outlines in Figure 3a mark the two sampled rows used for canopy validation.

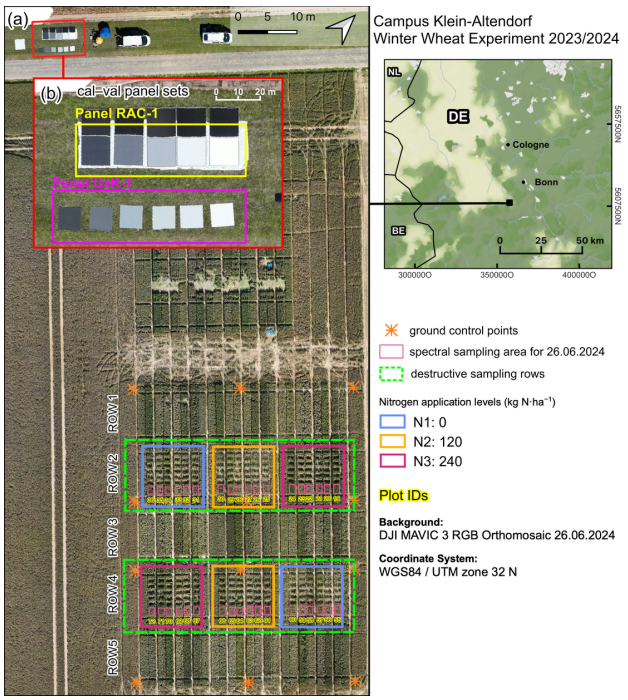

Figure 2. Study site and in-scene reference targets at Campus Klein-Altendorf near Bonn, Germany: (a) RGB orthomosaic of the winter wheat experiment, including GCPs, sampled rows, and plot layout; (b) detail of the two independent panel sets used for calibration (RAC-1) and validation (UzK-1). The inset map indicates the site location.

The field campaign represents one site and one acquisition window near solar noon under a clear sky over winter wheat. This setup isolates the radiometric transfer performance and cross-sensor consistency under controlled field conditions; however, it does not encompass the full range of canopy architectures, soil background contributions, or illumination/view-geometry combinations that may occur across crops or phenological stages. Accordingly, the protocol itself is intended to be transferable, whereas the canopy-level agreement metrics reported herein should be interpreted as performance under the tested winter wheat conditions.

All subsequent radiometric analyses were performed using the band-specific orthomosaics shown in Figure 3. The ELC was fitted separately for each band at flight altitude using RAC-1 imagery to convert digital numbers to reflectance, following established practices (Daniels et al., 2023). For the band-equivalent camera–ASD comparison, ASD spectra were harmonized with the camera bands using proxy spectral response functions (SRFs) modeled as Gaussians with FWHM matched to the nominal filter bandwidths because system-level SRFs were unavailable (Cundill et al., 2015). As panel and canopy spectra in the 980–1650 nm region are locally smooth and the passbands are narrow (nominal 10–12 nm FWHM), these proxy SRFs closely approximate band-equivalent reflectance (differences $\leq 10^{-3}$) and are sufficient for this analysis.

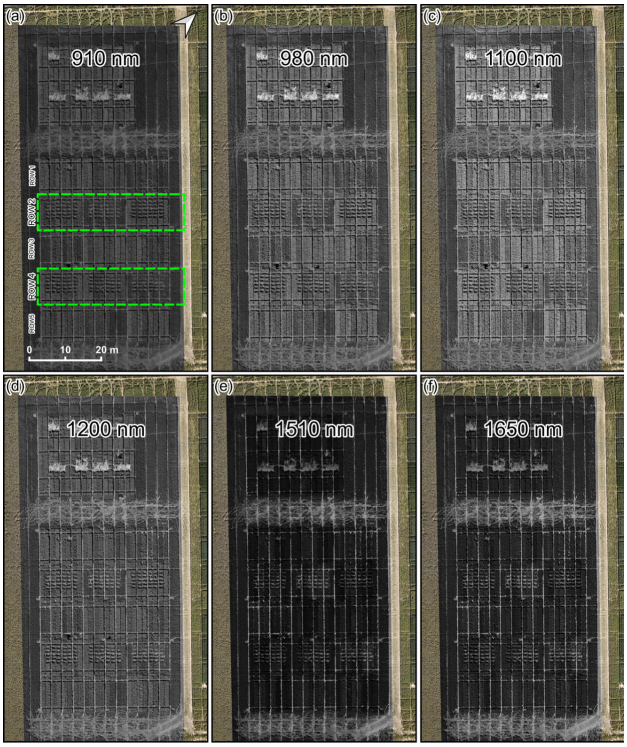

Figure 3. Georeferenced per-band reflectance orthomosaics derived from the six simultaneously exposed channels: (a) 910 nm, (b) 980 nm, (c) 1100 nm, (d) 1200 nm, (e) 1510 nm, and (f) 1650 nm. The mosaics show the same winter wheat trial as in Figure 2 and served as the basis for the ROI-based extraction of panel and canopy reflectance. The dashed outlines in (a) indicate the two sampled rows (rows 2 and 4) used for canopy validation.

As a sensitivity analysis, the camera–ASD comparison was repeated using both center-sampled ASD reflectance and Gaussian-convolved ASD reflectance to test whether the proxy-SRF assumption materially influenced the regression metrics. Camera-derived reflectance (y) was regressed against proxy-SRF-convolved ASD reflectance (x) by ordinary least squares (OLS), treating ASD as a reference measurement for evaluating camera consistency. We ran Theil–Sen and RANSAC as robustness checks; both returned parameters essentially indistinguishable from OLS without improving residual statistics; therefore, only OLS results are reported. For all regressions, we report slope and intercept (±SE), coefficient of determination (R^2), and sample size n. For ELC calibration fits (DN versus panel reflectance), RMSE denotes residual error about fitted calibration line. For independent panel validation, canopy-level camera–ASD comparisons, and Normalized Ratio Indices (NRI) comparisons, RMSE, MAE, bias, and MAPE are computed from direct difference between camera-derived value and corresponding reference value; they quantify deviation from 1:1 agreement rather than scatter about fitted regression. In addition to single-band validation, we computed two-band NRIs:

$$\mathrm{NRI}[\text{band 1, band 2}] = \frac{\rho_{\text{band1}} - \rho_{\text{band2}}}{\rho_{\text{band1}} + \rho_{\text{band2}}} \quad (1)$$

This contribution has been peer-reviewed. The double-blind peer-review was conducted on the basis of the full paper.
https://doi.org/10.5194/isprs-annals-XI-1-2026-61-2026

where ρ_{band1} and ρ_{band2} are the reflectance factors of the respective narrow bands (Koppe et al., 2010). Water- and protein-sensitive absorptions were targeted for the (1100, 1200) and (1650, 1510) pairs, as reported in the literature (Serrano et al., 2002; Herrmann et al., 2010; Roberts et al., 2018).

To further diagnose the non-compliant 910 nm channel, the stand-alone 910 nm bandpass element was characterized separately in the laboratory using an ASD FieldSpec 4 High-Res and a quartz–tungsten–halogen (QTH) lamp reflected from a diffuse white reference surface under fixed geometry. A reference spectrum was first acquired without the filter, after which the filter was inserted into the optical path, and a second spectrum was recorded. The relative spectral transmittance was computed as the ratio of filtered to unfiltered ASD digital numbers as a function of wavelength. The resulting curve was used exclusively as a component-level diagnostic of filter blocking behavior. It was not used as a system-level spectral response function (SRF) for cross-sensor harmonization because the optics, detector quantum efficiency, and incidence-angle effects were not included.

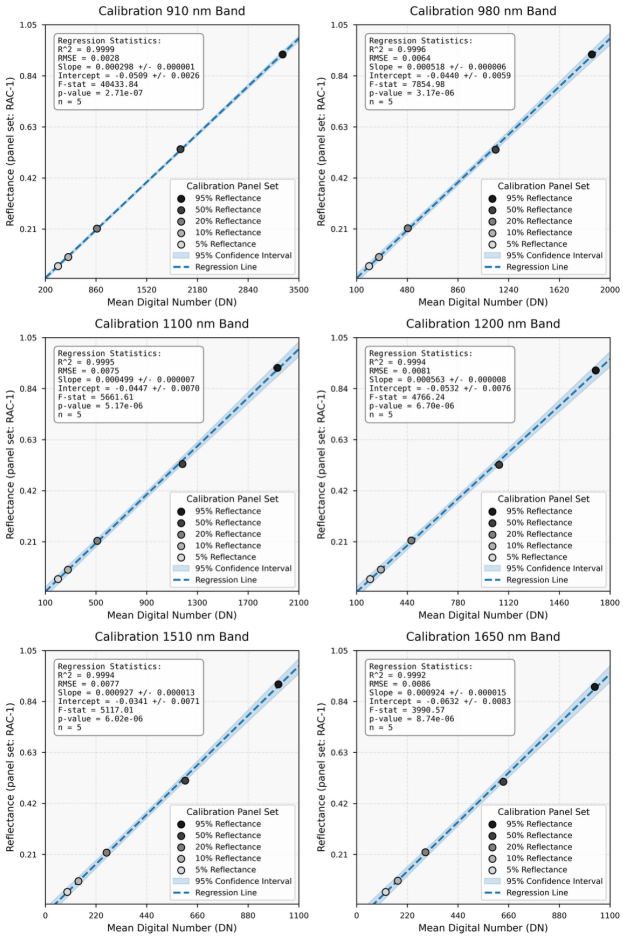

Figure 4. Empirical line calibration results for six VNIR–SWIR channels. For each band, the mean digital number (DN) measured over five reference panels (RAC-1; n = 5 gray levels) was regressed against laboratory-traceable panel reflectance to derive the linear DN-to-ρ transform. Because the fit uses large, homogeneous panel ROIs and only five discrete reflectance levels, R^2 approaches unity and is less diagnostic than the fitted calibration coefficients and the residual RMSE about the regression line.

3. Results

In-flight empirical line calibrations with RAC-1 at flight altitude exhibited $R^2 > 0.999$ and residual RMSE = 0.003–0.009 across all six bands. Near-perfect R^2 values are expected in this panel-based ELC setting because the regressions use the mean DN extracted over large, homogeneous panel ROIs and only five discrete reflectance levels; therefore, random scatter is very low under stable illumination. For this DN-to-reflectance transfer, more informative diagnostics are the fitted calibration coefficients and the residual RMSE about the fitted line, rather than R^2 alone. Across bands, the fitted intercepts were small and negative (−0.03 to −0.09 reflectance units), consistent with stable dark-level and straylight contributions that were absorbed by the calibration and did not impair subsequent retrieval because the panel gray levels spanned the canopy reflectance range (Figure 4) (Smith and Milton, 1999).

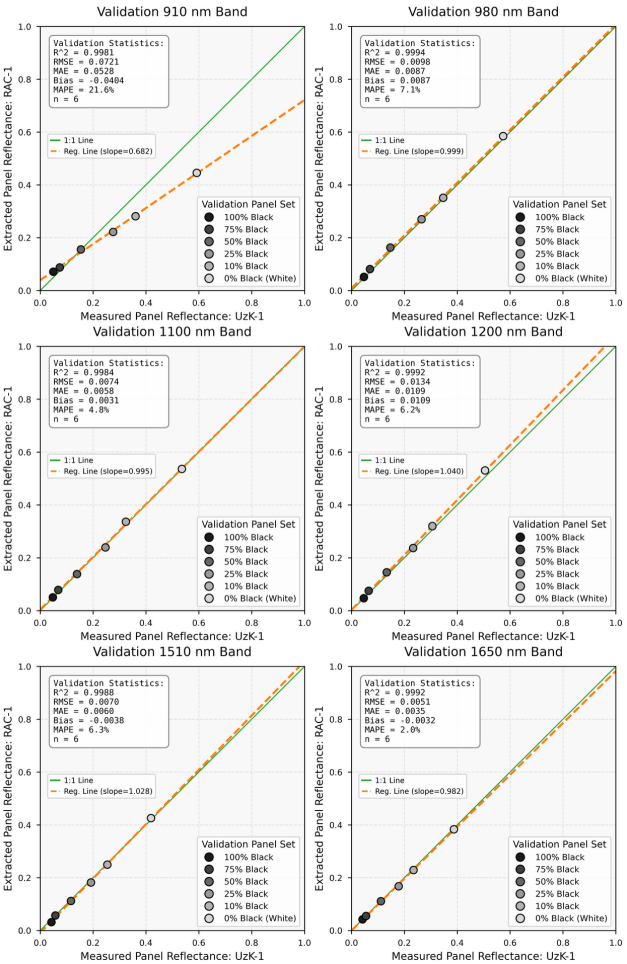

Figure 5. Independent panel validation using the second panel set (UzK-1; n = 6 gray levels) on RAC-1-calibrated orthomosaics. For each band, the reflectance extracted from the calibrated orthomosaics was plotted against the laboratory-traceable reflectance of the validation panels. Because the validation targets are homogeneous and span six discrete gray levels, R^2 is expected to be very high; deviations from unity slope, offsets, and absolute error metrics (RMSE/MAE/bias) provide the primary diagnostics of residual calibration error.

This contribution has been peer-reviewed. The double-blind peer-review was conducted on the basis of the full paper.
https://doi.org/10.5194/isprs-annals-XI-1-2026-61-2026 | © Author(s) 2026. CC BY 4.0 License.

Figure 5 shows the use of the UzK-1 validation panel set (six gray levels per band) as independent targets on RAC-1-calibrated orthomosaics. As expected, for a controlled target set with low within-panel variance, R^2 values are close to unity; deviations from unity slope, offsets, and absolute error metrics therefore provide more discriminative diagnostics than R^2 alone. The validation confirmed near-unity slopes and small offsets across 980–1650 nm, with high determination and low errors (e.g., slopes ≈ 0.999, 0.995, 1.040, 1.028, and 0.982 at 980, 1100, 1200, 1510, and 1650 nm; R^2 ≈ 0.998–0.999; RMSE ≈ 0.005–0.013), whereas the 910 nm band deviated substantially (slope = 0.682; RMSE = 0.072; MAPE = 21.6%), consistent with the identified out-of-band leakage. Because both calibration (RAC-1) and validation (UzK-1) were referenced to pre-characterized, laboratory-traceable panel reflectance factors (rather than in-field ASD panel readings), this design avoids closed-loop dependency between the spectroradiometer and the radiance-to-reflectance transfer while preserving the interpretability of the subsequent camera–ASD cross-sensor comparisons.

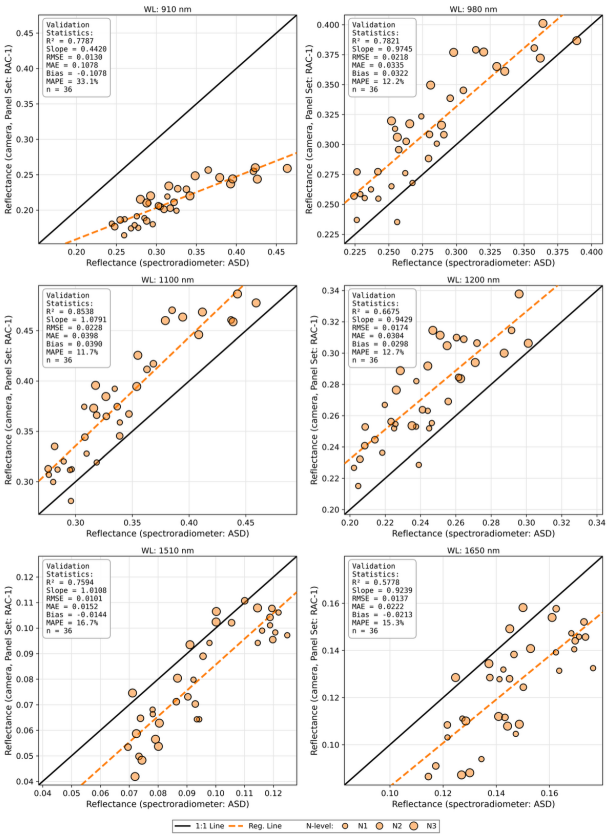

Figure 6. Plot-scale cross-sensor regressions (camera vs. spectroradiometer). For each band, the reflectance extracted from the RAC-1 ELC-calibrated camera mosaics (y-axis) was regressed against the band-equivalent reflectance from field spectroradiometer (ASD; x-axis) measurements.

At the plot level (36 canopy ROIs; SRF-matched ASD on the x-axis), five bands between 980 and 1650 nm achieved near-unity slopes with small intercepts, and R^2 = 0.58–0.85 with RMSE = 0.010–0.023 reflectance units. Specifically, at 980 nm and 1510 nm, the values were close to unity (slope = 0.974 ± 0.088; intercept = 0.039 ± 0.025 and slope = 1.011 ± 0.098; intercept = −0.015 ± 0.009, respectively). The 1100 nm band showed slight expansion (slope = 1.079 ± 0.077; intercept = 0.012 ± 0.026), whereas 1200 nm and 1650 nm were mildly compressed (slope = 0.943 ± 0.114; intercept = 0.044 ± 0.028 and slope = 0.924 ± 0.135; intercept = −0.010 ± 0.020). The intercept values remained small ($|b| \leq 0.044$). In contrast, at 910 nm, severe compression and bias were observed (slope = 0.442 ± 0.040; intercept = 0.071 ± 0.013; MAPE ≈ 33%), and therefore, this band was excluded from the accuracy claims. These relationships are illustrated in the six-panel scatterplot grids in Figure 6. Theil–Sen and RANSAC regressions returned slopes and intercepts within the OLS confidence bounds and offered no residual improvement, confirming the absence of leverage-driven outliers; therefore, we report only OLS estimates.

The two SWIR NRIs also showed strong cross-sensor agreement. In the RAC-1 ELC-calibrated mosaics shown in Figure 7, NRI[1100,1200] yielded R^2 ≈ 0.928, RMSE ≈ 0.010, slope ≈ 1.10, and intercept ≈ −0.020, whereas NRI[1650,1510] yielded R^2 ≈ 0.899, RMSE ≈ 0.018, slope ≈ 1.23, and intercept ≈ −0.043. Thus, both index relationships remained tight, albeit with modest gain expansion relative to the 1:1 line. This behavior is consistent with previous work showing that ratioing suppresses illumination variability and absorbs small per-band offsets, thereby preserving rank-order contrasts relevant to canopy water and protein signals (Crusiol et al., 2022).

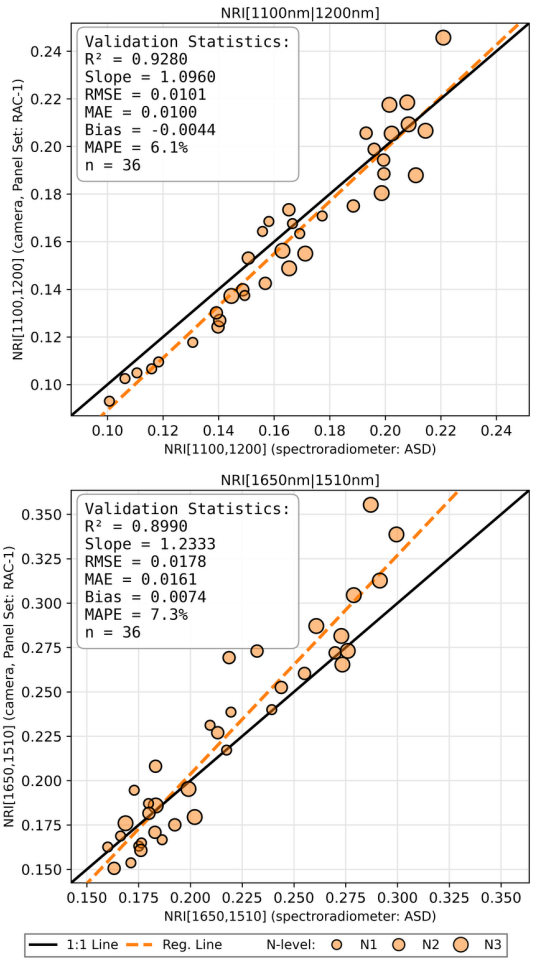

Figure 7. Plot-scale cross-sensor validation of SWIR normalized ratio indices (NRI) for the RAC-1 ELC-calibrated mosaics. Left: NRI[1100,1200]. Right: NRI[1650,1510]. Camera-derived NRI values (y-axis) were regressed against the corresponding NRI values computed from ASD spectroradiometer spectra after convolution to the camera bandpasses (x-axis). The black line denotes 1:1 agreement; the dashed orange line denotes the OLS fit.

This contribution has been peer-reviewed. The double-blind peer-review was conducted on the basis of the full paper.
https://doi.org/10.5194/isprs-annals-XI-1-2026-61-2026

Repeating the camera–ASD comparisons with and without SRF weighting (center-sample vs. Gaussian-convolved ASD) produced nearly identical regression metrics, with absolute differences in reflectance on the order of 10^{-4}–10^{-3}; this indicates that Gaussian SRF proxies at 10–12 nm FWHM are sufficient, consistent with the spectral smoothness of canopy reflectance in the narrow passbands of the camera.

A separate laboratory characterization of the stand-alone 910 nm bandpass element provided direct evidence for the suspected leakage mechanism (see Figure 8). The relative transmittance curve shows the intended narrow passband near 906–907 nm with a peak transmission of approximately 86%, but also an approximate onset of secondary long-wavelength throughput at 1196 nm. Because this secondary throughput overlaps the wavelength range to which the enhanced InGaAs detector remains sensitive, the 910 nm channel is not spectrally isolated from longer-wavelength scene contributions. This observation is consistent with the strong slope compression and elevated percentage errors found for the 910 nm channel in both the panel and canopy validations.

4. Discussion

The calibration–validation chain shows that the in-scene, multi-level ELC applied at flight altitude yields high-fidelity radiometric transfer (Ortiz et al., 2017; Daniels et al., 2023), with RAC-1 fits characterized by $R^2 \approx 1.0$, RMSE ≤ 0.009, and small negative intercepts consistent with dark-level offsets (Smith and Milton, 1999). Because the panel gray levels span the canopy reflectance range, these offsets do not impair quantitative retrieval (Sampath et al., 2023). Validating the material-distinct UzK-1 panel set on the RAC-1-calibrated orthomosaics produced unity-like slopes and low RMSE across five bands, indicating that the ELC behaved robustly across the two near-Lambertian panel materials and sizes tested and suggesting limited material-specific transfer bias (Bruegge, 1993; Schunke et al., 2023).

By anchoring the ELC and panel validation to laboratory-traceable panel reflectance factors instead of in-field ASD panel readings, we removed the potential closed-loop dependency between the spectroradiometer and radiance-to-reflectance transfer. Although this design may introduce small uncertainties from environmental and angular panel effects, the observed near-unity slopes and low RMSE values indicate that any independence penalty is negligible.

At the canopy scale (36 plots), the five compliant bands showed near-unity slopes, small intercepts ($|b| \leq 0.044$), and RMSE values of 0.010–0.023 reflectance units. The residual spread, especially the lower R^2 values at 1200 and 1650 nm, likely reflects BRDF and view-illumination effects in complex wheat canopies (Burkart et al., 2015; Comar et al., 2012), minor footprint mismatch between image and field spectra, and sensor noise (Sampath et al., 2023; Daniels et al., 2023) rather than spectral sampling differences, which are negligible after SRF convolution.

Although the panel-anchored ELC and SRF-aware comparison workflow is not crop-specific, canopy-level agreement metrics vary between vegetation types owing to canopy architecture, BRDF effects, leaf biochemical composition, and soil background exposure across crops and phenological stages. Radiometric transfer can remain linear and stable; however, the observed camera-to-spectroradiometer scatter at the canopy level may change as scene anisotropy and within-ROI heterogeneity change. Therefore, these results establish the quantitative performance of winter wheat under the tested conditions, and multicrop testing is a natural next validation step.

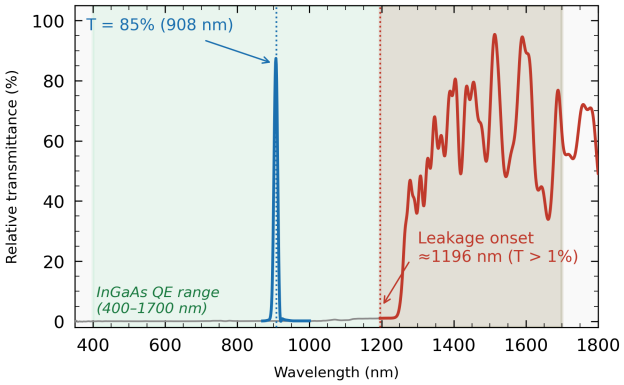

Figure 8. Relative transmittance of the stand-alone 910 nm bandpass filter measured with an ASD FieldSpec 4 (QTH reference). Besides the nominal passband near 906–907 nm, the filter exhibits secondary long-wavelength throughput beginning at ~1196 nm within the enhanced InGaAs sensitivity range. The measurement is shown as a component-level diagnostic and not a system-level SRF.

The Gaussian proxy SRFs (10–12 nm FWHM) had no material effect on the outcomes because (i) vegetation reflectance in the 980–1650 nm windows is locally smooth at this scale, (ii) the passbands are narrow and well separated from steep atmospheric features, and (iii) panel and canopy spectra lack sharp lines that are sensitive to small SRF shape differences. Consequently, the center-sampled vs. SRF-convolved ASD reflectance differed by $\leq 10^{-3}$, far below other error sources (radiometric transfer residuals, BRDF, and spatial mismatch).

The two SWIR ratio indices remained robust ($R^2 \approx 0.90$–0.93; RMSE $\approx$ 0.010–0.018) because normalization cancels illumination variability and absorbs small per-band offsets (Roberts et al., 2018). Specifically, NRI[1100,1200] emphasizes short-wave water–cellulose interactions, whereas NRI[1650,1510] couples protein-sensitive 1510 nm absorption with a nearby 1650 nm C–H overtone linked to plant biochemistry. These SWIR pairs target, in combination, complementary water and biochemical variations (Serrano et al., 2002; Herrmann et al., 2010; Roberts et al., 2018; Li et al., 2023; Chopra et al., 2025). By operating in the SWIR domain, these indices also complement VNIR indices (e.g., NDVI), which are prone to saturation at high LAI values (Jackson, 2004; Roberts et al., 2018).

Against this backdrop, the 910 nm channel consistently deviated from the expected behavior. For the RAC-1-calibrated orthomosaics evaluated with UzK-1 panels, we observed a slope of 0.682 with RMSE = 0.072 and MAPE = 21.6%. At the canopy level, the camera–ASD regression yielded a slope of 0.442 ± 0.040 and an intercept of 0.071 ± 0.013, with MAPE ≈ 33%. The sign and structure of the error, a negative bias relative to the ASD despite a positive intercept, indicate scale compression rather than a simple offset.

Laboratory transmittance measurements of the 910 nm bandpass element reveal incomplete long-wavelength blocking (Figure 8). The curve shows a passband centered near 906–907 nm with high transmission, plus a secondary long-wavelength throughput starting at 1196 nm. In an enhanced InGaAs system, this reopening occurs within the detector-sensitive range and allows longer-wavelength photons to contribute to the 910 nm channel. After ELC, this parasitic contribution is absorbed into the calibration but does not co-vary correctly with true 910 nm reflectance over vegetation, yielding compressed slopes and systematic biases relative to the SRF-convolved ASD reference. Leakage acts as a spectrally distinct additive term that varies with

This contribution has been peer-reviewed. The double-blind peer-review was conducted on the basis of the full paper.
https://doi.org/10.5194/isprs-annals-XI-1-2026-61-2026 | © Author(s) 2026. CC BY 4.0 License.

longer-wavelength absorptions in the 1200–1700 nm region. Because ELC cannot distinguish in-band from leaked photons, the fitted relationship bakes in crosstalk, reduces contrast, and produces slopes $\ll 1$, with errors growing when canopy spectra differ from calibration panels.

This laboratory ASD/QTH characterization documents the standalone filter element and should not be interpreted as the effective system SRF. The effective in-camera response depends on the optics, detector quantum efficiency, and incidence angle-dependent filter behavior. However, the secondary throughput within the detector-sensitive range explains the non-compliance of the 910 nm channel and supports its exclusion from quantitative accuracy claims.

Given the persistence of sub-unity slopes and elevated percentage errors, we excluded 910 nm from our accuracy claims and treated it as an engineering item for subsequent iterations. In line with this, Theil–Sen and RANSAC produced identical results to OLS, implying that residuals are well-behaved and that leverage/outliers do not drive the fits, apart from the designated 910 nm non-compliance, which is of spectral rather than robustness origin.

These findings for the 910 nm channel provide essential guidance for adopting enhanced InGaAs sensors in combined VNIR–SWIR systems. Our quantitative characterization revealed a fundamental limitation: long-wavelength contamination when applying silicon-optimized bandpass filters across 400–970 nm in enhanced InGaAs systems. Although these filters are adequate for silicon sensors with 1100 nm cutoffs, they require redesign for enhanced InGaAs detectors sensitive to 1700 nm. This requirement is not evident from standard filter specifications, which typically report blocking to 1200 nm, consistent with silicon sensor requirements. The documented slope compression (0.442 ± 0.040 for canopies and 0.682 for panels) and elevated percentage errors (MAPE $\approx 33\%$ for vegetation) offer benchmarks for filter specifications in future implementations. These empirical lessons show that to fully exploit the extended 400 nm sensitivity of improved InGaAs sensors while maintaining radiometric fidelity, this long-wavelength leakage must be overcome through appropriate measures, particularly when implementing narrow bands below 970 nm, where silicon-heritage filter designs prove insufficient.

The most practical mitigation is to add a short-pass element with a high optical density (OD) to the 910 nm optical path (target OD 5–6 blocking from 1000 to 1700 nm); alternatively, a custom bandpass with a specified long-wave blocking is required. Multilayer interference filters shift toward shorter wavelengths as the incidence angle increases, and their passband shape changes under converging beams and varying chief-ray angles. Accordingly, blocking performance must be verified for actual in-camera geometry rather than normal-incidence bench conditions (Baker and Yen, 1967; Rienstra, 1998). Stacking a high-OD short-pass filter with a 910 nm bandpass would reduce residual long-wave leakage across the detector-sensitive 1200–1700 nm range and make the channel response more robust across field angles. Verification should rely on in situ system-level SRFs (filter × optics × detector) with field-angle sampling and bench checks against the specified blocking performance (Pagnutti et al., 2025). Until a functional solution is implemented, bandpass filters with center wavelengths ≤ 970 nm should be treated as conditional engineering bands rather than as quantitative reflectance bands. For subsequent deployments, bands with center wavelengths ≤ 970 nm were replaced with higher-center-wavelength filters (> 970 nm).

5. Conclusion and Outlook

This study demonstrates that a modular, filter-reconfigurable enhanced-InGaAs UAV payload can deliver quantitative reflectance and robust SWIR indices at the plot scale for the five compliant bands between 980 and 1650 nm when paired with panel-anchored empirical line calibration (ELC) and SRF-aware cross-sensor comparison.

At flight altitude, the ELC fit on the RAC-1 calibration panel set was near-perfect, and independent validation on the UzK-1 panel set returned unity-like slopes and low errors for the five compliant bands between 980 and 1650 nm. Over winter wheat canopy plot ROIs ($n = 36$), these bands showed slopes close to one, small intercepts, $R^2 \approx 0.58$–0.85, and RMSE ≈ 0.010–0.023, while robust estimators agreed with OLS, indicating well-behaved residuals. Two SWIR normalized-ratio indices (NRI[1100,1200] and NRI[1650,1510]) showed tight cross-sensor agreement ($R^2 \approx 0.90$–0.93), consistent with their resilience to illumination and small per-band offsets. The 910 nm band was non-compliant, where bandpass filter leakage compressed the dynamic range (panel slope ≈ 0.68; canopy slope ≈ 0.44) and elevated errors; thus, we excluded it from accuracy claims and specified remedies (higher-OD short-pass blocking, stacked filters, and system-level SRF measurements, including off-axis checks). The study confirms that the self-developed VNIR–SWIR payload can produce quantitative reflectance and agronomic SWIR indices at centimeter-level resolution when calibrated with a panel-anchored ELC and compared with bandpass-aware harmonization. This provides an engineering path to rehabilitate narrow bands ≤ 970 nm without undermining the performance of the 980–1650 nm bands.

A limitation is that validation covered only winter wheat in one campaign; therefore, the reported agreement metrics quantify performance under these conditions, whereas broader robustness across crops, phenological stages, and environmental conditions requires further demonstration.

Based on these conclusions, we aim to extend the spectral blocking range for bands ≤ 970 nm to eliminate long-wavelength leakage without sacrificing throughput. Laboratory transmittance measurements of the 910 nm element show that blocking for enhanced InGaAs implementations must extend beyond 1200 nm across the detector-sensitive 1200–1700 nm interval to prevent VNIR bands from reopening to longer-wavelength contamination. To unlock the enhanced potential of InGaAs sensors, we will introduce stronger short-pass blocking to produce leakage-free bandpass-selectable bands in the VNIR that complement the 980–1650 nm bands. We will translate reflectance into agronomy through multivariate within-season time series and multi-year campaigns spanning different cultivars and nitrogen treatments across crop types and contrasting acquisition conditions (e.g., illumination, phenological stages, and soil background exposure). These efforts will relate the validated bands and SWIR indices to plot-scale traits and assess accuracy across seasons while maintaining lightweight protocols.

To extend the platform capability from canopy monitoring to joint soil–canopy assessment, particularly under partial cover in the early growing season, we will complement the SWIR payload with a calibrated VNIR multispectral sensor, providing spectral information needed for soil–vegetation discrimination. This extension will enable the evaluation of soil-focused visible indices, such as the soil organic carbon index (SOCI; Thaler et al., 2019), over exposed soil and mixed scenes and support the interpretation of plot-scale variability when soil background affects measurements. These steps aim to convert the prototype into a robust VNIR–SWIR platform for quantitative plot-scale agronomy and vegetation monitoring on aerial platforms.

This contribution has been peer-reviewed. The double-blind peer-review was conducted on the basis of the full paper.
https://doi.org/10.5194/isprs-annals-XI-1-2026-61-2026 | © Author(s) 2026. CC BY 4.0 License.

Acknowledgements

Thuy Nguyen was funded by the German Federal Ministry of Education and Research (BMBF) through the Digital Agriculture Knowledge and Information System (DAKIS2) Project [Grant number 031B1524B]. Thuy Nguyen also thanks the Deutsche Forschungsgemeinschaft (DFG, German Research Foundation) under Germany's Excellence Strategy-EXC 2070-390732324 (PhenoRob).

References

Aasen, H., Honkavaara, E., Lucieer, A., Zarco-Tejada, P. J., 2018. Quantitative Remote Sensing at Ultra-High Resolution with UAV Spectroscopy: A Review of Sensor Technology, Measurement Procedures, and Data Correction Workflows. *Remote Sensing*, 10(7), 1091, doi.org/10.3390/rs10071091.

Anderson, M. C., Neale, C. M. U., Li, F., Norman, J. M., Kustas, W. P., Jayanthi, H., Chavez, J., 2004. Upscaling ground observations of vegetation water content, canopy height, and leaf area index during SMEX02 using aircraft and Landsat imagery. *Remote Sensing of Environment*, 2002 Soil Moisture Experiment (SMEX02), 92(4), 447–464, doi.org/10.1016/j.rse.2004.03.019.

Baker, M. L., Yen, V. L., 1967. Effects of the variation of angle of incidence and temperature on infrared filter characteristics. *Applied Optics*, 6(8), 1343–1351, doi.org/10.1364/AO.6.001343.

Berger, K., Verrelst, J., Féret, J.-B., Wang, Z., Wocher, M., Strathmann, M., Danner, M., Mauser, W., Hank, T., 2020. Crop nitrogen monitoring: Recent progress and principal developments in the context of imaging spectroscopy missions. *Remote Sensing of Environment*, 242, 111758, doi.org/10.1016/j.rse.2020.111758.

Bruegge, C. J., 1993. Use of Spectralon as a diffuse reflectance standard for in-flight calibration of earth-orbiting sensors. *Optical Engineering*, 32(4), 805, doi.org/10.1117/12.132373.

Burkart, A., Aasen, H., Alonso, L., Menz, G., Bareth, G., Rascher, U., 2015. Angular Dependency of Hyperspectral Measurements over Wheat Characterized by a Novel UAV Based Goniometer. *Remote Sensing*, 7(1), 725–746, doi.org/10.3390/rs70100725.

Chakhvashvili, E., Machwitz, M., Antala, M., Rozenstein, O., Prikaziuk, E., Schlerf, M., Naethe, P., Wan, Q., Komárek, J., Klouek, T., Wieneke, S., Siegmann, B., Kefauver, S., Kycko, M., Balde, H., Paz, V. S., Jimenez-Berni, J. A., Buddenbaum, H., Hänchen, L., … Rascher, U., 2024. Crop stress detection from UAVs: Best practices and lessons learned for exploiting sensor synergies. *Precision Agriculture*, 25(5), 2614–2642, doi.org/10.1007/s11119-024-10168-3.

Chander, G., Mishra, N., Helder, D. L., Aaron, D. B., Angal, A., Choi, T., Xiong, X., Doelling, D. R., 2013. Applications of Spectral Band Adjustment Factors (SBAF) for Cross-Calibration. *IEEE Transactions on Geoscience and Remote Sensing*, 51(3), 1267–1281, doi.org/10.1109/TGRS.2012.2228007.

Chopra, Y., Xie, X., Clothier, J., Ghosh, S., Yu, H., Walia, H., Sattler, S. E., 2025. Hyperspectral imaging to characterize the vegetative tissue biochemical changes in response to water deficit conditions in sorghum (Sorghum bicolor). *Frontiers in Plant Science*, 16, doi.org/10.3389/fpls.2025.1515998.

Comar, A., Baret, F., Viénot, F., Yan, L., de Solan, B., 2012. Wheat leaf bidirectional reflectance measurements: Description and quantification of the volume, specular and hot-spot scattering features. *Remote Sensing of Environment*, 121, 26–35. doi.org/10.1016/j.rse.2011.01.028.

Crusiol, L. G. T., Sun, L., Sun, Z., Chen, R., Wu, Y., Ma, J., Song, C., 2022. In-Season Monitoring of Maize Leaf Water Content Using Ground-Based and UAV-Based Hyperspectral Data. *Sustainability*, 14(15), 9039, doi.org/10.3390/su14159039.

Cundill, S., Van Der Werff, H., Van Der Meijde, M., 2015. Adjusting Spectral Indices for Spectral Response Function Differences of Very High Spatial Resolution Sensors Simulated from Field Spectra. *Sensors*, 15(3), 6221–6240, doi.org/10.3390/s150306221.

Daniels, L., Eeckhout, E., Wieme, J., Dejaegher, Y., Audenaert, K., Maes, W. H., 2023. Identifying the Optimal Radiometric Calibration Method for UAV-Based Multispectral Imaging. *Remote Sensing*, 15(11), 2909, doi.org/10.3390/rs15112909.

Gao, B., 1996. NDWI—A normalized difference water index for remote sensing of vegetation liquid water from space. *Remote Sensing of Environment*, 58(3), 257–266, doi.org/10.1016/S0034-4257(96)00067-3.

Herrmann, I., Karnieli, A., Bonfil, D. J., Cohen, Y., Alchanatis, V., 2010. SWIR-based spectral indices for assessing nitrogen content in potato fields. *International Journal of Remote Sensing*, 31(19), 5127–5143, doi.org/10.1080/01431160903283892.

Honkavaara, E., Eskelinen, M. A., Pölönen, I., Saari, H., Ojanen, H., Mannila, R., Holmlund, C., Hakala, T., Litkey, P., Rosnell, T., Viljanen, N., Pulkkanen, M., 2016. Remote Sensing of 3-D Geometry and Surface Moisture of a Peat Production Area Using Hyperspectral Frame Cameras in Visible to Short-Wave Infrared Spectral Ranges Onboard a Small Unmanned Airborne Vehicle (UAV). *IEEE Transactions on Geoscience and Remote Sensing*, 54(9), 5440–5454, doi.org/10.1109/TGRS.2016.2565471.

Hunt, E. R., Daughtry, C. S. T., 2018. What good are unmanned aircraft systems for agricultural remote sensing and precision agriculture? *International Journal of Remote Sensing*, 39(15–16), 5345–5376, doi.org/10.1080/01431161.2017.1410300.

Jackson, T., 2004. Vegetation water content mapping using Landsat data derived normalized difference water index for corn and soybeans. *Remote Sensing of Environment*, 92(4), 475–482. doi.org/10.1016/j.rse.2003.10.021.

Jenal, A., Bareth, G., Bolten, A., Kneer, C., Weber, I., Bongartz, J., 2019. Development of a VNIR–SWIR Multispectral Imaging System for Vegetation Monitoring with Unmanned Aerial Vehicles. *Sensors*, 19(24), 5507. doi.org/10.3390/s19245507

Jenal, A., Hütt, C., Reddig, F., Bolten, A., Bareth, G., Bongartz, J., 2024. Expanding horizons: Introducing a 6-channel VNIR-SWIR multicamera system for advanced UAV-based remote sensing applications. *DGPF-Jahrestagung 2024*, 32, 385–393, doi.org/10.24407/KXP:1885709293.

Koppe, W., Li, F., Gnyp, M. L., Miao, Y., Jia, L., Chen, X., Zhang, F., Bareth, G., 2010. Evaluating Multispectral and Hyperspectral Satellite Remote Sensing Data for Estimating Winter Wheat Growth Parameters at Regional Scale in the North China Plain. *Photogrammetrie - Fernerkundung - Geoinformation*, 2010(3), 167–178, doi.org/10.1127/1432-8364/2010/0047.

Lee, I., Kim, H.-W., Kim, Y., Ahn, H., Ryu, J.-H., Jeong, H., 2024. Spatiotemporal monitoring of soybean growth and water status using drone-based shortwave infrared (SWIR) imagery. *Korean Journal of Remote Sensing*, 40, 275–284, doi.org/10.7780/kjrs.2024.40.3.4.

Li, X., Peng, F., Wei, Z., Han, G., Liu, J., 2023. Non-destructive detection of protein content in mulberry leaves by using hyperspectral imaging. *Frontiers in Plant Science*, 14, doi.org/10.3389/fpls.2023.1275004.

Lu, H., Fan, T., Ghimire, P., Deng, L., 2020. Experimental Evaluation and Consistency Comparison of UAV Multispectral Minisensors. *Remote Sensing*, 12(16), 2542, doi.org/10.3390/rs12162542.

Maes, W. H., Steppe, K., 2019. Perspectives for Remote Sensing with Unmanned Aerial Vehicles in Precision Agriculture. *Trends in Plant Science*, 24(2), 152–164, doi.org/10.1016/j.tplants.2018.11.007.

Marshall, M., Belgiu, M., Boschetti, M., Pepe, M., Stein, A., Nelson, A., 2022. Field-level crop yield estimation with PRISMA and Sentinel-2. ISPRS Journal of Photogrammetry and *Remote Sensing*, 187, 191–210, doi.org/10.1016/j.isprsjprs.2022.03.008.

Mutanga, O., Skidmore, A. K., 2004. Narrow band vegetation indices overcome the saturation problem in biomass estimation. *International Journal of Remote Sensing*, 25(19), 3999–4014, doi.org/10.1080/01431160310001654923.

Mutanga, O., Masenyama, A., Sibanda, M., 2023. Spectral saturation in the remote sensing of high-density vegetation traits: A systematic review of progress, challenges, and prospects. *ISPRS Journal of Photogrammetry and Remote Sensing*, 198, 297–309, doi.org/10.1016/j.isprsjprs.2023.03.010.

Nansen, C., Lee, H., Mantri, A., 2023. Calibration to maximize temporal radiometric repeatability of airborne hyperspectral imaging data. *Frontiers in Plant Science*, 14, 1051410, doi.org/10.3389/fpls.2023.1051410.

Oliveira, R. A., Näsi, R., Korhonen, P., Mustonen, A., Niemeläinen, O., Koivumäki, N., Hakala, T., Suomalainen, J., Kaivosoja, J., Honkavaara, E., 2023. High-precision estimation of grass quality and quantity using UAS-based VNIR and SWIR hyperspectral cameras and machine learning. *Precision Agriculture*, 25, 186–220, doi.org/10.1007/s11119-023-10064-2.

Ortiz, J. D., Avouris, D., Schiller, S., Luvall, J. C., Lekki, J. D., Tokars, R. P., Anderson, R. C., Shuchman, R., Sayers, M., Becker, R., 2017. Intercomparison of Approaches to the Empirical Line Method for Vicarious Hyperspectral Reflectance Calibration. *Frontiers in Marine Science*, 4, doi.org/10.3389/fmars.2017.00296.

Pagnutti, M., Ryan, R. E., Frommeyer, J., Cuervo, D., Sitton, D., 2025. Methods, procedures, and example results for evaluating commercial off-the-shelf hyperspectral instruments for use as satellite cross-calibration radiometers. *Journal of Applied Remote Sensing*, 19(2), 027501, doi.org/10.1117/1.JRS.19.027501.

Rienstra, J. L., 1998. Transformation of filter transmission data for f-number and chief ray angle. In: Infrared Imaging Systems: Design, Analysis, Modeling, and Testing IX. *Proceedings of SPIE*, 3377, 267–275, doi.org/10.1117/12.319380.

Roberts, D. A., Roth, K. L., Wetherley, E. B., Meerdink, S. K., Perroy, R. L., 2018. Hyperspectral Vegetation Indices. In *Hyperspectral Indices and Image Classifications for Agriculture and Vegetation*. CRC Press, doi.org/10.1201/9781315159331-1.

Sampath, A., Shrestha, M., While, M., Scholl, V. M., 2023. Guidelines for calibration of uncrewed aircraft systems imagery. *U.S. Geological Survey*, Open-File Report, 2023–1033, doi.org/10.3133/ofr20231033.

Schunke, S., Leroy, V., Govaerts, Y., 2023. Retrieving BRDFs from UAV-based radiometers for fiducial reference measurements: Caveats and recommendations. *Frontiers in Remote Sensing*, 4, doi.org/10.3389/frsen.2023.1285800.

Serrano, L., Peñuelas, J., Ustin, S. L., 2002. Remote sensing of nitrogen and lignin in Mediterranean vegetation from AVIRIS data: Decomposing biochemical from structural signals. *Remote Sensing of Environment*, 81(2), 355–364, doi.org/10.1016/S0034-4257(02)00011-1.

Sims, D. A., Gamon, J. A., 2003. Estimation of vegetation water content and photosynthetic tissue area from spectral reflectance: A comparison of indices based on liquid water and chlorophyll absorption features. *Remote Sensing of Environment*, 84(4), 526–537, doi.org/10.1016/S0034-4257(02)00151-7.

Smith, G. M., Milton, E. J., 1999. The use of the empirical line method to calibrate remotely sensed data to reflectance. *International Journal of Remote Sensing*, 20(13), 2653–2662, doi.org/10.1080/014311699211994.

Thaler, E. A., Larsen, I. J., Yu, Q., 2019. A New Index for Remote Sensing of Soil Organic Carbon Based Solely on Visible Wavelengths. *Soil Science Society of America Journal*, 83(5), 1443–1450, doi.org/10.2136/sssaj2018.09.0318.

Thompson, D. R., Boardman, J. W., Eastwood, M. L., Green, R. O., Haag, J. M., Mouroulis, P., Van Gorp, B., 2018. Imaging spectrometer stray spectral response: In-flight characterization, correction, and validation. *Remote Sensing of Environment*, 204, 850–860, doi.org/10.1016/j.rse.2017.09.015.

Trishchenko, A. P., Cihlar, J., Li, Z., 2002. Effects of spectral response function on surface reflectance and NDVI measured with moderate resolution satellite sensors. *Remote Sensing of Environment*, 81(1), 1–18, doi.org/10.1016/S0034-4257(01)00328-5.

Yang, G., Liu, J., Zhao, C., Li, Z., Huang, Y., Yu, H., Xu, B., Yang, X., Zhu, D., Zhang, X., Zhang, R., Feng, H., Zhao, X., Li, Z., Li, H., Yang, H., 2017. Unmanned Aerial Vehicle Remote Sensing for Field-Based Crop Phenotyping: Current Status and Perspectives. *Frontiers in Plant Science*, 8, 1111, doi.org/10.3389/fpls.2017.01111.